Romanian Reports in Physics **72**, 502 (2020)

EFFECT OF Mn SUBSTITUTION ON THE STRUCTURAL, MAGNETIC AND MAGNETOSTRICTIVE PROPERTIES OF Fe-Pd FERROMAGNETIC SHAPE MEMORY RIBBONS

M. SOFRONIE*, M. ENCULESCU, A.D. CRISAN, F. TOLEA

National Institute of Materials Physics, Atomistilor 405A, 077125, Magurele, Romania
E-mails: *mdatcu@infim.ro, alina.crisan@infim.ro, felicia.tolea@infim.ro*
* Corresponding author: *mihsof@infim.ro*

Received July 2, 2019

Abstract. This work reports the effect of the Mn substitution, rapid solidification technique and heat treatments on the martensitic transformation, magnetic and magnetostrictive properties on the $Fe_{70-x}Pd_{30}Mn_x$ (x = 1, 3) ferromagnetic shape memory ribbons. The samples were investigated by X-ray diffraction, differential scanning calorimetry, scanning electron microscopy, magnetic and magnetostrictive measurements. The thermal treatments induce significant changes in the microstructure and magnetocrystalline anisotropy of the martensitic phase, for $Fe_{67}Pd_{30}Mn_3$ compared to $Fe_{69}Pd_{30}Mn_1$. The competition between the magnetization orientation and twin boundary motion within martensitic variants under magnetic field evidenced in the magnetic-strain curves was discussed and correlated with the magnetic data.

Key words: ferromagnetic shape memory alloys, martensitic transformation, magnetostriction.

1. INTRODUCTION

The ferromagnetic shape memory alloys (FSMA) are very attractive materials for devices development required in engineering application, due to their shape change in external magnetic fields. The large strains are induced by applied magnetic field in the martensitic phase, by twin variants reorientation and twin boundary motion. The phenomenon differs from the conventional magnetostriction, where the magnetic moments rotate to field direction without changing the unit cell orientation [1]. The Fe-Pd FSMA is a promising material compared to well-known Ni-Mn-Ga [2] due to better mechanical properties and high Curie temperature (~760 K), although the magnetic field-induced strains have lower values [3–4]. By cooling, the Fe-Pd (~30 at.% Pd) alloy suffers a thermo-elastic and reversible martensitic transformation (MT) from face-centered cubic (FCC) austenite to face-centered tetragonal (FCT) martensite; by further cooling, the irreversible MT FCT-BCT (body-centered tetragonal) may be evidenced. In order to stabilize the FCT martensite, *i.e.* to avoid the formation of the undesirable BCT martensite and to manipulate the transformation temperatures, the addition of a third alloying element (Ni, Pt, Co, Rh, Mn, Cu) in Fe-Pd system was used [5–13]. The investigation of the Fe-Pd-Mn ternary bulk system shows the

increase of reversible MT temperatures (~333 K) and decrease of the irreversible ones. The highest MT temperatures (~379 K) were reported for $Fe_{64.3}Pd_{29}Mn_{6.7}$ thin film. Rapid solidification, by using a melt-spinning technique, is an effective processing route to obtain this alloy as ribbons in which the high temperature FCC structure can be frozen as single phase [7]. The materials produced as thin ribbons are ideally shaped for sensors designs.

Previously reported data have shown that MT temperatures are influenced by the fabrication method and Mn substitution improves the FSMA properties of Fe-Pd (30 at.% Pd) alloy [13]. To our knowledge, there are no previously reported studies on Fe-Pd-Mn ribbons obtained by melt spinning technique. The present work aims to study the effect of Mn addition and heat treatments on the structural, magnetic and magnetostriction properties of $Fe_{70-x}Pd_{30}Mn_x$ (x = 1, 3) melt-spun ribbons, in the perspective of using these materials for applications.

2. EXPERIMENTAL

The ingots of $Fe_{70-x}Pd_{30}Mn_x$ (x = 1, 3) alloys were prepared by arc-melting (under Ar protective atmosphere) of high purity elements, the procedure being repeated several times to ensure homogeneity. Afterwards, the ingots were melt-spun into ribbons, with 3 mm wideness, 10–20 mm lengthiness and 25–30 μm thickness, (Copper wheel velocity – 20 m/s, 50 kPa Ar overpressure, crucible nozzle diameter – 0.5 mm). The "as-prepared" ribbons were subsequently treated in vacuum quartz ampoules at 950^{o}C for different duration. The samples were denoted Mnx-y, where x-Mn content (at.%) and y-length of thermal treatment (TT): 0, 10 and 30 minutes. Each treatment was followed by direct quenching of samples in iced water.

The MT parameters were determined by using the differential scanning calorimetry (DSC) (model 204 F1 Phoenix-Netzsch, with scanning rate – 10 K/min). The structural investigations were done by X-ray diffraction (XRD) using a Bruker D8 Advantage diffractometer in the Bragg-Brentano geometry, with Cu Kα radiation, at different temperatures. The chemical composition and the surface morphology were examined by Energy Dispersive X-Ray Spectroscopy (EDX) and Scanning Electron Microscopy (SEM) in a Zeiss Evo 50 XVP microscope, at room temperature (RT). Magnetic measurements were performed by MPMS-SQUID-QD magnetometer, with magnetic field along to the ribbon direction. The strain *versus* magnetic field measurements were achieved by using the strain gauges method. In-plane strains, with the field applied parallel and transverse to ribbons were recorded at different temperatures.

3. RESULTS AND DISCUSSIONS

In order to evidence MT, a first DSC scan has been performed in wide temperature range (90–400 K), for all samples. It is important to note the absence of

the irreversible martensitic transformation, as result of the melt spinning technique. A second scan was restricted to the temperature range of interest (200–350 K), in order to describe and detail the specific MT parameters: martensite and austenite start (Ms, As) and finish (Mf, Af) temperatures, the transformation enthalpy (*H*), calculated as average between the direct and reverse enthalpy (Table 1).

Table 1

The MT characteristic temperatures – martensite start (Ms) and finish (Mf), austenite start (As) and finish, (Af) – the transformation enthalpy (*H*), calculated as average between the direct and reverse enthalpy. The temperatures determined from the thermomagnetic measurements are marked with (*)

Sample	**Ms // Mf [K]**	**As // Af [K]**	***H* [J/g]**
Mn1-0	315 // 303 275 // 268	304 // 316 272 // 277	0.023 0.07
Mn1-10	281 // 275	282 // 286	0.11
Mn1-30	284 // 279	283 // 288	0.22
Mn3-0	263* // 247*	255* // 275*	–
Mn3-10	322 // 307	312 // 335	0.97
Mn3-30	320 // 305	310 / /326	0.34

The Mn substitution causes an unusual behavior of as prepared ribbons compared to $Fe_{70}Pd_{30}$ ribbons [14]. A two-stage reversible transformation with very low enthalpy values appears, due to atomic disorder and wide distribution of grain sizes, resulting from the melt-spinning technique. Moreover, MT was not detected by DSC measurements for Mn3-0 as-prepared ribbons, probably due to its wide temperature range and very low enthalpy. The data marked with (*) (Table 1) have been obtained from the thermomagnetic measurements. After TTs, exists only one-stage MT with drastic increase of start martensitic temperature (Ms) up to 322 K for Mn3-10 ribbons, close to that achieved for thin films (Ms = 335 K) with the same concentration [13].

The X-ray diffraction patterns of as-prepared ribbons with different Mn content indicate a single FCC phase, the high temperature stable phase retained in the ribbons due to the rapid cooling [7]. Since the atomic radius for Mn (0.140 nm) is higher than Fe (0.126 nm) and Pd (0.137 nm), an increase of lattice constant (a_0 = 0.373 nm for FCC structure of $Fe_{70}Pd_{30}$ ribbons [14]) when adding Mn should occur. Indeed, the crystal lattice constant increases with Mn content [0.374 nm (Mn1-0) – 0.375 nm (Mn3-0)]. After TTs, RT X-ray diffraction patterns on Mn1-10 and Mn1-30 samples (not show) indicate the peaks sharpening due to the atomic ordering. For 3 at.% Mn content, in concordance with the DSC results, both TT samples have a mixture of austenite (FCC) and martensite (FCT) with small content of another phase rich in Pd and Mn (@). Figure 1 shows the X-ray diffraction profiles recorded on Mn3-10 sample at different temperatures. The sample was cooled from 100°C, step by step (~20°C) to –100°C, in martensitic phase.

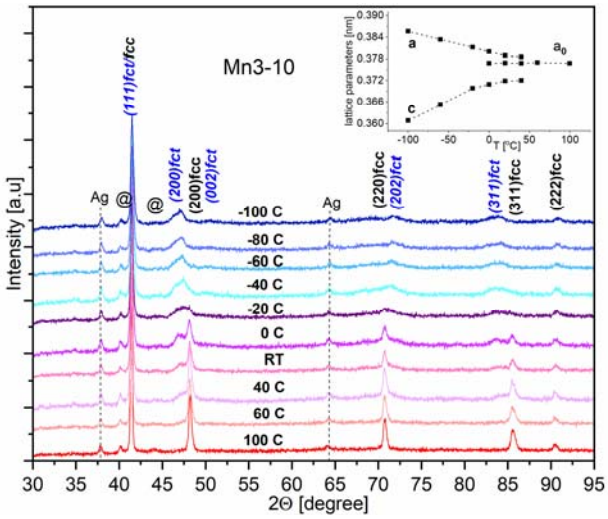

Fig. 1 – X-ray diffraction profiles recorded at different temperatures for Mn3-10 sample. Inset: the evolution of the lattice parameters with temperature, a_0 of the cubic austenite and a and c of the tetragonal martensite (the dashed lines are guide for the eye).

By cooling, the intensity of the FCC characteristic diffraction peaks decreases until them disappear, being replaced by those denoting the FCT structure. In addition, a secondary phase with the diffraction peaks marked with (@) and the sample holder glue peaks (Ag-show with dashed lines) are evidenced. The Inset Fig. 1 shows the lattice parameters evolution with the temperature for Mn3-10 ribbons, highlighting the MT features, specific to Fe-Pd FSMA. So, the coexistence of the austenite and martensite reveals a first-order transformation, while the continuous development of the tetragonality suggests a second order phase transformation. A sudden jump of c/a ratio from 1 to 0.982 appears at 40°C (close to Ms) and attain 0.936 at –100°C, close to 0.94 reported for Fe-Pd (30 at.% Pd) alloys, at same temperature [1].

The free surface (surface without contact with copper wheel) (Fig. 2) and cross-section ribbons morphology (Fig. 3a–b) have been analyzed by scanning electron microscopy (SEM), at RT. For Mn1-y ribbons the images indicate grains with different size (2–10 μm), without martensitic relief, the MT being below RT (not show). Figure 2a shows grains with various shape and dimension, starting from 450 nm and reaching up to 7 μm, the mean size being estimated at 1 μm, for Mn3-0 sample. Seki *et al.* [15] reveal that for Fe-Pd polycrystalline samples, the MT temperatures are very sensitive to this small grains size and decrease fast. The martensitic microstructure is observed on some grains with higher size, indicating that the MT starts at room temperature, even it wasn't detected by calorimetric measurements.

After TT at 950°C for 10 min, the SEM image shows larger grains (2–10 μm) and on some of it is observed the twin variants morphology specific to martensite,

attesting the coexistence of austenite and martensite, observed in the XRD diffraction pattern at RT (Fig. 2b). Also, many precipitates (0.5–1 μm) appear largely at the boundaries of the grains, but not only. The second TT (30 min at 950°C) promotes a continuous growth of the grains (4–20 μm), the biggest ones seem to clustered (Fig. 2c). On their surface rarely appears the martensitic microstructure and it is obvious that new precipitates nucleate and growth besides the existing ones. In enlarged image (300 nm) (Fig. 2d) of one of these grains can be observed some twin variants which are "arrested" between precipitates, the MT being obstructed. This assumption is supported by the small transformation enthalpy value (0.34 J/g) for Mn3-30 sample (Table 1).

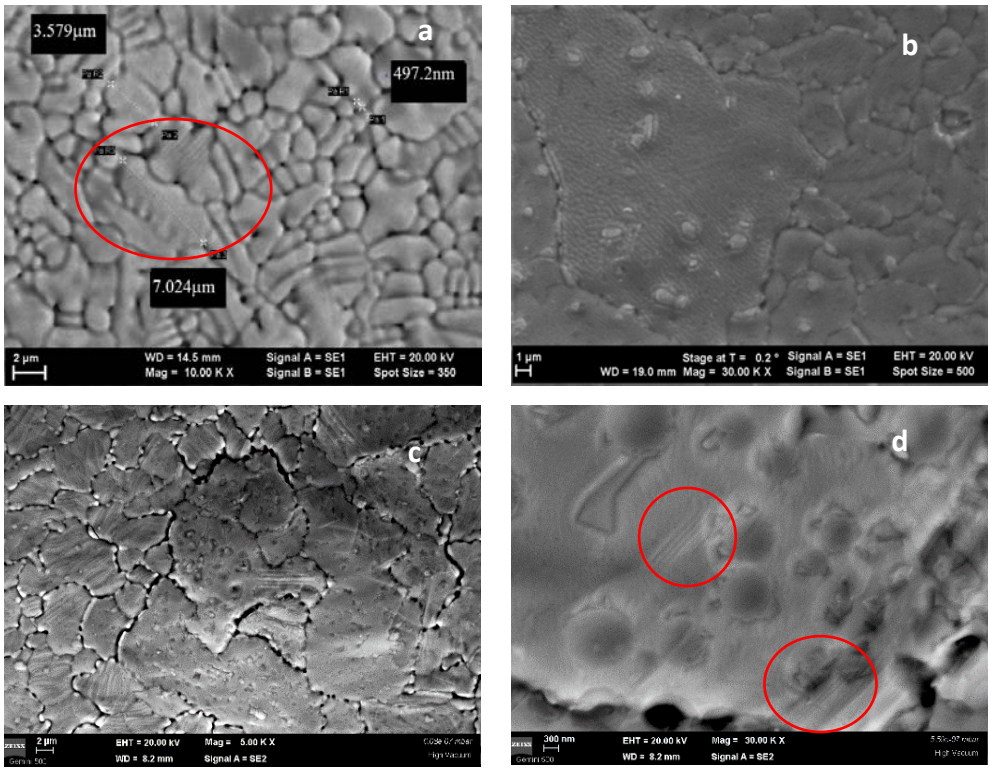

Fig. 2 – The SEM images for Mn3-0 (a), Mn3-10 (b) and Mn3-30 (c–d) samples.

The chemical compositions were carried out by EDX microanalysis. The compositions for Mn1-*y* and Mn3-0 samples were the nominal ones (within the limits of the method accuracy). Differences from nominal composition were observed for Mn3-10 and Mn3-30 samples and are related to the presence of precipitates. Table 2 shows the elemental chemical composition for the matrix and precipitates, calculated as average of the values obtained on three different points.

Table 2

The chemical compositions, calculated as average of values obtained on three different sample's points, for Mn3-10 and Mn3-30 ribbons

Sample		Fe (at.%)	Pd (at.%)	Mn (at.%)
Mn3-10	average	66.52	30.44	3.03
	matrix	70.05	27.79	2.16
	precipitates	43.22	41.23	16.15
Mn3-30	average	66.31	30.38	3.31
	matrix	68.61	29.17	2.22
	precipitates	45.45	39.66	14.12

The cross-section images show a "sponge-like" structure with random equiaxial grains for Mn1-*y* ribbons (Fig. 3a) and a columnar structure with small intercalated precipitates, for Mn3-10 ribbons (Fig. 3b). It is supposed that these precipitates may represent the secondary phase, marked with @, in the XRD pattern for Mn3-10 (Fig. 1).

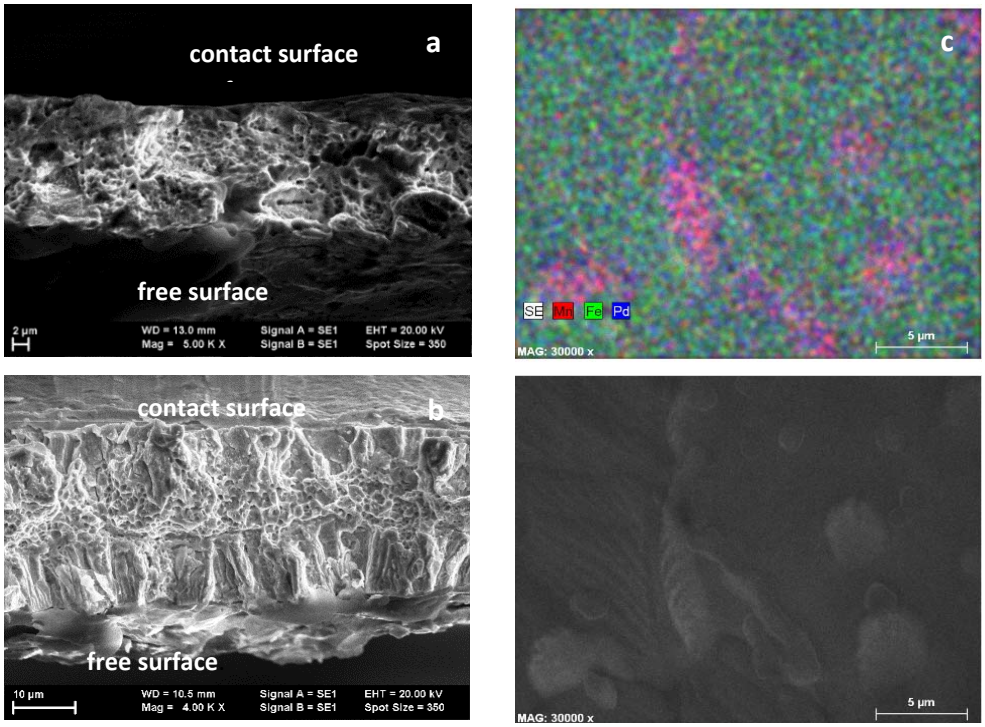

Fig. 3 – The SEM cross-section images of Mn1-10 (a) and Mn3-10 (b) samples (contact surface is the ribbon surface in contact with copper wheel); The mapping of the Mn3-30 ribbon free surface (c).

The elemental mapping of the Mn3-30 ribbon surface (Fig. 3c) confirms the precipitates enriched with Mn and Pd embedded in a homogenous matrix and attests the low solubility of Mn in the Fe-Pd system [12]. It should be noted that the

reduction of Pd content in the matrix for Mn3-10 and Mn3-30 ribbons, can justify the increase of the MT temperatures, taking into account that these are very sensitive to the Pd concentration in Fe-Pd FSMA [16].

The thermomagnetic measurements were performed in constant magnetic field (300 Oe) by cooling from 390 K to 200 K, well below to MT temperature and warming them up again (Fig. 4). On cooling, at low field, due to its higher magnetocrystalline anisotropy, the martensitic phase is more difficult to be magnetized than the austenite one, that giving rise to the magnetization drop, by passing from austenite to martensite. After the cooling/heating sequence, the magnetization returns to the same values, which confirms the absence of the irreversible MT. Figure 4a shows the two-stage MT for Mn1-0 sample at close temperatures indicated by calorimetric measurements and one-stage MT at increased temperature (~10 K) after TTs (Inset Fig. 4a).

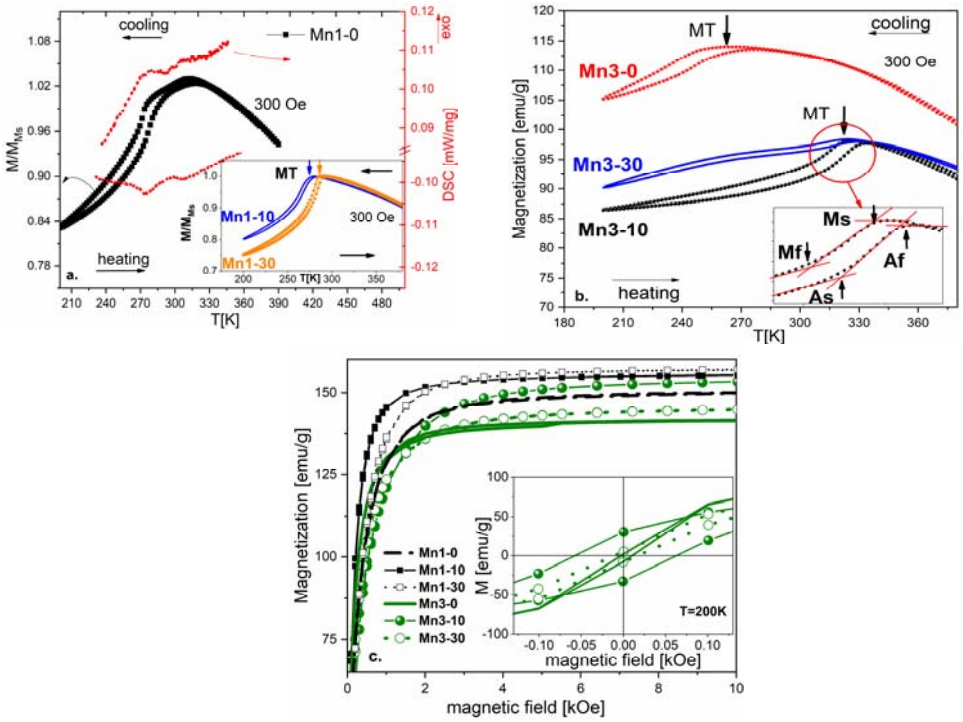

Fig. 4 – Temperature dependences of relative magnetization and calorimetric measurement (M/M_{Ms}, where M_{Ms} is the magnetization at M_s temperature) at constant magnetic field (300 Oe) for Mn1-0 sample (a) (Inset: Temperature dependences of relative magnetization for Mn1-10 and Mn1-30); Thermomagnetic curves on cooling/heating sequence for Mn3-*y* samples (300 Oe) (b); Magnetic isotherms in martensitic state (200K) for Mn1-*y*, Mn3-*y* (c) (Inset: the magnetic hysteresis loops for Mn3-*y* samples at 200 K).

At lower temperatures (M_s = 263K) was achieved MT for Mn3-0 sample and its characteristic values were obtained by method indicated into zoom image (Fig. 4b).

The SEM image (Fig. 2a) shows on some grains the martensitic microstructure, even at room temperature, therefore can be presuming a very wide MT for Mn3-0 sample. The atomic ordering and matrix composition change due to nucleation and growing of precipitates, increase the MT temperatures with ~ 60 K for Mn3 TTs samples. In-plane magnetization curves measured in martensitic phase (200 K) up to 10 kOe were achieved (Fig. 4c), for all samples. First, was confirmed the magnetization decrease with Mn content, similar with Fe-Pd-Mn bulk alloy [12], for as-prepared samples. Second, the TTs induce very small increase of the saturation magnetization for 1% at Mn samples (Fig. 4c). Contrary, can be distinguished the difference between saturation magnetization, closely related to the matrix concentration of Fe (Table 2), for 3 at.% Mn TTs samples. In martensitic state (200 K), Mn3-10 gains higher saturation magnetization value than Mn3-30. Moreover, a wide hysteresis loop with increased coercive field (H_c ~ 65 Oe) were obtained for Mn3-10 sample, a signature of the magnetocrystalline anisotropy improvement (Inset Fig. 4c).

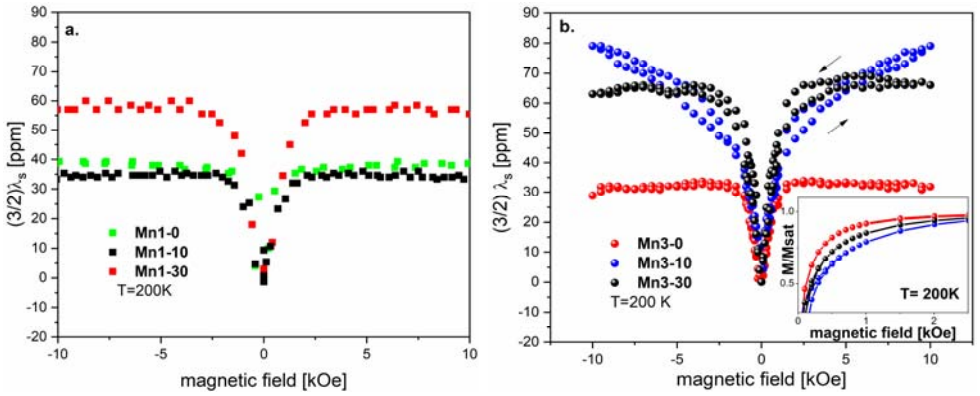

Fig. 5 – The magnetostriction isotherm in martensitic state (200 K) for Mn1-*y* (a) and Mn3-*y* (b) ribbons (Inset: Relative magnetization *versus* magnetic field for Mn3-*y* at 200 K).

The plane-strains recorded with magnetic fields up to 10 kOe applied along (parallel strains – λ_p) and transverse (λ_t) (perpendicular to the thickness) to the ribbons length (at 200 K), allow to study the saturation magnetostriction coefficient (λ_s) by using relation $(3/2)\lambda_s = \lambda_p - \lambda_t$ [17]. For the Mn1-*y* ribbons the magnetostriction reach saturation in low fields (~2.5 kOe), takes moderate values and are not significant enhanced by the thermal treatments (Fig. 5a). Our results are in good agreement with previous reported data on Fe-Pd prepared as ribbons [14]. A different behavior is evidenced on Mn3-10 ribbons, the magnetostriction does not saturate up to 10 kOe and shows hysteresis. Such type of dependence suggests the martensitic variants reorientation. For the variants reorientation, their elastic and frictional energies involved in this process must be surpassed by the magnetic anisotropy energy. The magnetic isotherms at 200 K shown in Fig. 4c and Insert Fig. 5b reveal that Mn3-10 has the highest magnetocrystalline energy. It is to note that for Mn3-10, SEM cross-section image reveals a clear columnar structure. In order to justify the

anisotropy of Mn3-10 ribbons one may take into account previously reported observations who signaled for columnar structure a preferential martensitic variants selection during the MT required by a bias stress [18] at the grain boundaries resulting always the short *c* axis aligned in plane perpendicular to the columnar grains. For Mn3-30 sample the nucleation and growth of the new precipitate of the secondary phase may partially damage the columnar structure, reduces the magnetic anisotropy and the martensitic variants reorientation is no longer possible.

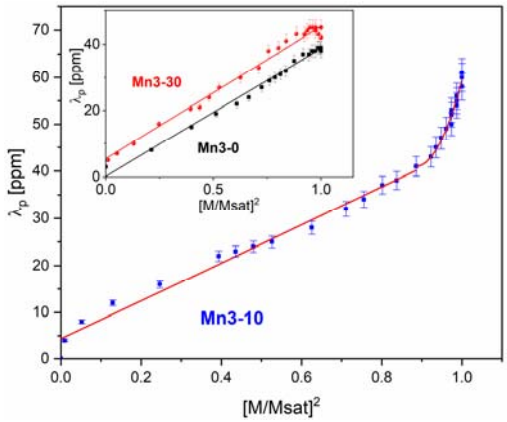

Fig. 6 – Magnetostriction plotted *versus* the relative magnetization square for Mn3-10 ribbon (Inset: Mn3-0, Mn3-30 ribbons).

Further, another method was applied to identify the mechanism responsible for the strain-magnetic field dependence; the parallel magnetostriction (λ_p) values collected at 200 K were plotted against the relative magnetization square $(M/M_{sat})^2$ (Fig. 6). The quadratic relation between the magnetization and magnetostriction given by $\lambda = (3/2)\lambda_s(M/M_{sat})^2$, M – field dependent magnetization, M_{sat} – saturation magnetization [19], indicates a rotational mechanism namely the rotation of the magnetic moments to the magnetic field direction without change the unit cell orientation. Inset Fig. 6 shows the linear dependence λ_p *vs.* $(M/M_{sat})^2$ and confirms the rotation mechanism of the magnetic moments in the martensitic variants, for Mn3-0 and Mn3-30 samples. For Mn3-10 ribbons, the same linear dependence is observed only in low fields, where the magnetic moments rotation is the main mechanism (Fig. 6). At higher fields, a deviation from linear dependence indicates other mechanism, probably the martensitic variants reorientation taking into account the arguments previously discussed.

4. CONCLUSIONS

The rapid solidification technique promotes the formation of single phase ribbons with high atomic disorder, without irreversible martensitic transformation

for Fe-Pd-Mn alloys. The Mn substitution induces a microstructure with very small grains which determinates a decrease of MT temperatures for as prepared ribbons. The sponge-like structure with equiaxed and columnar grains was evidenced for 1% Mn, respective 3% Mn ribbons. The thermal treatments induce a moderate increase of MT temperatures and transformation enthalpy for $Fe_{67}Pd_{30}Mn_1$ samples.

In case of $Fe_{67}Pd_{30}Mn_3$, a short thermal treatment at high temperature assists the occurrence of a secondary phase which changes the matrix composition, that contribute essentially to significant increase of MT temperature. Moreover, this thermal treatment induces the improved of the magnetocystalline anisotropy of the martensitic state and allows higher magneto-strain values unsaturated at 10 kOe. The magneto-strain behavior indicates the rotation mechanism at low field, followed by variant reorientation mechanism at higher field. Further thermal treatment favors the second phase increase which damages the columnar structure, reduces the magnetic anisotropy and the martensitic variants reorientation disappears.

Acknowledgments. The authors thank PhD. M Valeanu for the useful discussions. This work was supported by Grant of Romanian Ministry of Research and Innovation, CCCDI-UEFISCDI, project number PN-III-P1-1.2-PCCDI-2017-0062/contract no.58/component project no. 2, within PNCDI III.

REFERENCES

1. J. Cui, T.W. Shield, R. D. James, Acta Mater. **52**, 35–47 (2004).
2. K. Ullakko, J. Mater Eng. Perform. **5**, 405–409 (1996).
3. R. Oshima, M. Sugiyama, J. Phys. Colloq. **C4**, 383–389 (1982).
4. S.G. Greculeasa, G. Schinteie, P. Palade, G. Filoti, I. S. Ghita, V. Kuncser, Rom. Rep. Phys. **68**, 249–258 (2016).
5. D. Vokoun, Y. W. Wang, T. Goryczka, C. T. Hu, Smart Mater. Struct. **14**, 261–265 (2005).
6. C. F. Lin, J.B. Yang, J. Magn. Magn. Mater. **322**, 197–207 (2010).
7. F. Tolea, M. Sofronie, J. Optoelectron. Adv. M. **20** 11–12, 701–706 (2018).
8. V. Sánchez-Alarcos, V. Recarte, J. I. Pérez-Landazábal, C. Gómez-Polo, V. A. Chernenko, M.A. González, Eur. Phys. J. Special Topics **158**, 107–112 (2008).
9. S. Hamann, M.E. Gruner, Acta Mater. **58**, 5949–5961 (2010).
10. M.E. Gruner, S. Hamann, H. Brunken, A. Ludwig, P. Entel, J. All. Compd. **577S**, S333–S337 (2013).
11. K. Tsuchiya, T. Nojiri, H. Ohtsuka, M. Umemoto, M. Mater. Trans. **12**, 2499–2502 (2003).
12. V. Sánchez-Alarcos, V. Recarte, J. I. Pérez-Landazábal, M.A. González, J.A. Rodriguez-Velamazán, Acta Mater. **57**, 4224–4232 (2009).
13. S. Hamann, A. Savan, S. Thienhaus, A. Ludwig, Proceedings of 11th Conf. on New Actuators, Bremen, Germany, 271 (2008).
14. M. Sofronie, F. Tolea, V. Kuncser, M. Valeanu, G. Filoti, IEEE Trans. Mag. **51**, 2500404 (2015).
15. K. Seki, H. Kura, T. Sato, T. Taniyama, J. App. Phys. **103**, 063910 (2008).
16. R. Oshima, Scripta. Metall. **15**, 829 (1981).
17. E. du Trémolet de Lacheisserie, *Magnetostriction: Theory and Applications of Magnetoelasticity*, CRC, Boca Raton, 1993.
18. I. Claussen, R.A. Brand, H. Hahn, S.G. Mayr, Scr. Mater. **66**,163–166 (2012).
19. E W Lee, Rep. Prog. Phys. **18**, 184 (1955).